Research Square

Preprints are preliminary reports that have not undergone peer review.
They should not be considered conclusive, used to inform clinical practice,
or referenced by the media as validated information.

Somatic Missense Mutations at the MCL-1 BH3-Binding Groove Paradoxically Enhance BAK Sequestration: Computational Evidence for Apoptotic Resistance

Raf Son Jany Rafad
Jashore University of Science and Technology
Tanay Chakrovarty
t.chakrovarty@just.edu.bd

Jashore University of Science and Technology
Humaira Anjume
Jashore University of Science and Technology
Deepanwita Chakraborty
University of Missouri
Maksuda Akter
Jashore University of Science and Technology
Fariha Biswas
Jashore University of Science and Technology
Md. Neyamul
Jashore University of Science and Technology
Mst. Marufa Afrin
Jashore University of Science and Technology

Article

Keywords: MCL-1, Somatic Missense Mutations, BAK Sequestration, BH3-binding groove, Precision oncology

Posted Date: May 28th, 2026

DOI: https://doi.org/10.21203/rs.3.rs-9825806/v1

License: This work is licensed under a Creative Commons Attribution 4.0 International License.
Read Full License

Additional Declarations: No competing interests reported.

Abstract

Myeloid cell leukemia (MCL-1) enhances the viability of tumor cells by sequestering the pro-apoptotic effector BAK within its BH3-binding groove. The structural and functional implications of somatic missense mutations at this contact are inadequately defined. We comprehensively investigated 146 somatic MCL-1 missense variations from the COSMIC database employing an array of *In-silico* tools. Utilizing SIFT, PolyPhen-2, PROVEAN, SNPs&GO, PANTHER, and MetaRNN, we discovered seven high-confidence detrimental variants: R215G, V216G, L235Q, R263S, G271D, W305G, and G311D. All seven mutations uniformly destabilized the MCL-1 monomer across six thermodynamic frameworks of which five variations are located at highly conserved locations. Protein–protein docking on five platforms indicated that five variations (R215G, V216G, L235Q, R263S, and G271D) establish MCL-1–BAK complexes with binding energetics superior to the wild type (PRODIGY ΔG = −12.8 kcal/mol). Molecular dynamics simulations (100 ns) demonstrated that V216G, L235Q, R263S, and G271D exhibited more compact hydrogen-bond-rich interfaces than the wild-type. R263S compensates for the absence of the Arg263 salt bridge by forming a stronger hydrogen-bond network. These results show that gain-of-interface contact is a computationally recognized mechanism by which cells can resist apoptosis. R263S and G271D are the best candidates for experimental confirmation and the creation of mutation-specific inhibitors.

1.0 Introduction

Apoptosis is a programmed cell death mechanism essential for maintaining cellular and immunological homeostasis by eliminating damaged or developmentally unnecessary cells. The intrinsic, or mitochondrial, apoptotic pathway serves as the principal regulatory mechanism, governed by interactions among members of the B-cell lymphoma 2 (BCL-2) protein family[1]. These tri-partite family of proteins: anti-apoptotic guardians BCL-2, BCL-XL, MCL-1, BCL-W, and A1/BFL-1, preserve mitochondrial integrity; pro-apoptotic effectors BAX and BAK, which promote membrane permeabilization; and BH3-only sensitizer, including BIM, PUMA, BAD, NOXA, and BMF, which relay upstream cellular stress signals to the effectors[2]. The balance among these groups at the mitochondrial outer membrane determines cell fate. Under homeostatic conditions, anti-apoptotic proteins sequester BAK and BAX within their canonical BH3-binding grooves, thereby inhibiting BAK/BAX homo-oligomerization and preventing mitochondrial outer membrane permeabilization (MOMP)[3]. When apoptotic signals overcome this inhibition, MOMP occurs, releasing cytochrome c into the cytosol, which triggers apoptosome formation and activates the caspase cascade, culminating in cell death[4].

Within the anti-apoptotic BCL-2 family, myeloid cell leukemia-1 (MCL-1) plays a pivotal role in promoting cancer cell survival[5–7]. MCL-1 is characterized by an extended, intrinsically disordered N-terminal domain containing PEST sequences that regulate its degradation, and a compact core forming a BH3-binding groove with four hydrophobic pockets (P1–P4) that accommodate BH3 helices from pro-apoptotic partners[8]. MCL-1 demonstrates high affinity for BAK, BIM, and NOXA proteins[9]. Elevated MCL-

1 expression is frequently observed in multiple myeloma, acute myeloid leukemia, and non-small cell lung cancer, often due to genetic alterations at locus 1q21[10]. Binding specificity studies show that BIM interacts with all anti-apoptotic proteins[11], NOXA selectively binds MCL-1[12], and BAD does not interact with MCL-1[13]. These binding patterns suggest that changes in MCL-1 activity can influence cell death sensitivity in various cell types.

MCL-1 gene amplification and transcriptional upregulation are established mechanisms of resistance[14]; however, somatic missense mutations represent a distinct and increasingly recognized form of oncogenic dysregulation[15]. These point mutations can alter the amino acid sequence of MCL-1 at structurally or functionally critical sites, potentially impacting protein folding, thermodynamic stability, and, most notably, the architecture of the BH3-binding groove that mediates BAK and BAX sequestration. Recent mutational analyses have identified pathogenic variants in the N-terminal PEST region (e.g., G32R and P142S) and in the BH domains (e.g., N223S, R214Q, V249L, and L267V)[16]. The BH1-domain variant L267V is particularly significant, as it confers resistance to potent clinical-stage MCL-1 inhibitors S63845 and AZD5991 by impeding their ability to disrupt the MCL-1–BAK interaction[16]. These findings indicate that specific amino acid changes within the groove can simultaneously reduce therapeutic binding while maintaining, or even enhancing, sequestration of pro-apoptotic proteins.

Previous structural and computational studies have begun to clarify the molecular consequences of MCL-1 mutations on interactions within the BCL-2 family[8]. Recently reported that the V220F substitution near the P3 groove induces a loop-to-helix conformational change in MCL-1, which enhances its interaction with BAX but destabilizes the MCL-1 monomer, establishing a model for gain-of-interface function resulting from thermodynamically disruptive mutations[17]. More recently, the molecular determinants of MCL-1/BAK interaction specificity at atomic resolution are defined, demonstrating that extensive hydrophobic and electrostatic interactions within the P1–P4 groove are key to high-affinity BAK sequestration and explaining how groove-targeted inhibitors compete with BAK BH3 for these binding sites[18].

Despite these advances, a comprehensive computational analysis of the full spectrum of somatic MCL-1 missense mutations—addressing their pathogenic potential, thermodynamic effects, evolutionary conservation, structural consequences, and quantitative impact on BAK binding affinity—remains lacking. This gap is clinically significant because mutations that strengthen the MCL-1–BAK interface represent a resistance mechanism undetectable by protein expression or gene amplification assays, thus requiring specialized structural computational approaches for identification. The present study applies an integrative in silico framework to systematically evaluate somatic MCL-1 missense variants catalogued in COSMIC[19], with the objectives of determining their pathogenicity and quantifying their influence on MCL-1–BAK binding affinity. The study aims to identify variants that modify the BH3-binding groove to enhance BAK sequestration, to elucidate the structural mechanisms underlying this gain-of-interface phenomenon, and to provide a structural rationale for precision oncology strategies targeting MCL-1-dependent malignancies.

2.0 Results

2.1 Acquisition of Protein Sequence and Missense Variant Data

After sequence acquisition, seven of 146 identified variants were chosen as most deleterious based on computational predictions and filtering (Supplementary file 1). These seven underwent detailed structural and functional analysis, described below.

2.2 Predicting the Functional Implications of Missense Variants

All 146 missense variants were assessed by three computational tools: SIFT, PolyPhen-2, and PROVEAN. SIFT found 84 harmful and 62 benign variants. PolyPhen-2 identified 17 likely harmful variants (score >0.98), 43 benign, and 23 potentially detrimental variants. One incorrect variant was excluded. PROVEAN then tested the 17, finding 7 to be detrimental (score < −4.5). The selected variants—R215G, V216G, L235Q, R263S, G271D, W305G, and G311D—were consistently marked as deleterious by all three tools and were moved forward for further study (Table 1). Predictions from two additional tools, SNPs&GO and PANTHER, also indicated that these polymorphisms are harmful (Table 1). PolyPhen-2 values ranged from 0.989 (R215G) to 1.000 (R263S, W305G). SIFT scores were from 0.000 to 0.013, where lower values indicate a higher probability of harm. PROVEAN delta scores ranged from −4.53 (G271D) to −12.08 (W305G), all meeting the −4.5 cutoff for detrimental impact. SNPs&GO marked six of seven as disease-associated (score >0.5), with R263S at 0.821; V216G was neutral (score = 0.468). PANTHER results were similar, with W305G highest (0.832) and G311D neutral (0.470). The convergence among these methods supports the choice of these seven variants.

2.3 Analysis of Protein Thermodynamic Stability

The thermodynamic effects of the seven variants on MCL-1 stability were assessed using four sequence-based computational tools: I-Mutant2.0, MUpro, SAAFEC, and iStable (Table 2). These tools predict changes in protein stability upon mutation by estimating ΔΔG (change in Gibbs free energy) values in kilocalories per mole (kcal/mol); negative ΔΔG values indicate destabilization, while positive values indicate increased stability. I-Mutant2.0 projected destabilizing ΔΔG values (<0 kcal/mol) for all mutations, from −1.60 kcal/mol (R215G, G271D) to −3.54 kcal/mol (V216G). MUpro found destabilization for six variants, except G271D, which had a positive score (+0.636). SAAFEC and iStable also showed destabilizing ΔΔG values for all, ranging from −1.17 kcal/mol (G271D) to −2.50 kcal/mol (W305G) and from 0.664 (W305G) to 0.756 (V216G), respectively. All results support that these seven mutations destabilize MCL-1.

2.4 Analysis of Evolutionary Conservation

The evolutionary conservation of wild-type MCL-1 protein residues was evaluated using ConSurf, which rates conservation from 1 (variable) to 9 (highly conserved) within protein families (Figure 2). Among the seven harmful variants, R215G and R263S were at highly conserved, exposed sites (scoring 9). V216G, G271D, and W305G were also highly conserved but buried inside the protein. L235Q and G311D had

fewer conserved sites. The fact that five variants are at the most conserved positions suggests they are essential, and mutations at these sites are likely to impair protein structure and function.

2.5 Comparative Structural Analysis of Wild-Type and Mutant Proteins

Structure-based predictions from mCSM and DynaMut2 (Table 3) agreed with those from sequence-based tools (Table 1). mCSM found all seven variants destabilizing; V216G (ΔΔG = −2.35 kcal/mol) and W305G (ΔΔG = −2.818 kcal/mol) were most affected. The remaining variants had destabilizing values from −0.763 (R215G) to −1.832 (R263S). DynaMut2 also indicated destabilization for all; W305G had the largest free-energy drop (ΔΔG = −2.90), with V216G next (ΔΔG = −2.28). Both methods flagged V216G and W305G as the most disruptive variants for protein stability.

2.6 Assessment of Structural Consequences of Point Mutations

Project HOPE found clear physical and chemical differences between wild-type and mutant side chains at all seven positions (Table 4). Four variants (R215G, V216G, R263S, and W305G) had shorter side chains than in the wild-type protein. L235Q, G271D, and G311D had larger side chains. Smaller side chains may disrupt bonding or protein packing, while larger side chains can cause steric clashes. MetaRNN pathogenicity scores ranged from 0.862 (V216G) to 0.982 (G311D), with all variants marked pathogenic. The combined changes in side-chain size and high MetaRNN scores identify these as likely harmful.

2.7 Analysis of Interaction Networks and Pathway Enrichment

GeneMANIA identified 20 human genes associated with MCL-1. Edges in the network map represent co-expression, physical interactions, shared pathways, co-localization, genetic interactions, and domain similarity (Figure 3A; Supplementary file 2). Main interactors included BAK1 (0.0054), BCL2L11 (0.0043), PMAIP1 (0.0022), BAX (0.0013), HUWE1 (0.00113), BCL2L1 (0.00076), and BCL2 (0.00062) (Supplementary file 2). STRING analysis yielded a confidence score of 0.999, identifying 10 MCL-1 interaction partners including BAK1, BAX, BCL2, and BCL2L1 (Figure 3B). Pathway enrichment analysis via WebGestalt identified seven main pathways among MCL1-related genes (Supplementary file 3). The top pathway was apoptosis (hsa04215; enrichment ratio = 106.82, $p = 1.48 \times 10^{-15}$, FDR = 5.19×10^{-13}). Other pathways included apoptosis (hsa04210), platinum drug resistance, p53 signaling, cancer pathways, colorectal cancer, and measles.

2.8 Structural Modeling and Validation of Mutant Proteins Using the Ramachandran Plot

Wild-type MCL-1 (PDB ID: 6OQB, 1.60 Å, X-ray crystallography; Figure 4A) and BAK (PDB ID: 7M5B, 1.85 Å, X-ray; Figure 4A) structures were retrieved from the Protein Data Bank. Seven MCL-1 missense variants were modeled in 3D using SWISS-MODEL. Templates were chosen based on GMQE and sequence coverage. PyMOL was used to visualize the mutant models (Figure 4B). Ramachandran plot validation using PROCHECK showed each model had 95.6% of residues in most favored regions (Figure 4C), meeting accepted modeling standards. All structures were validated before docking experiments.

2.9 Molecular Docking of Proteins

Molecular docking was performed for the seven MCL-1 variants with wild-type BAK using five platforms, with the wild-type MCL-1–BAK complex serving as baseline (Table 5). The wild-type complex had a binding free energy of ΔG = −16.17 kcal/mol and a dissociation constant of Kd = 1.38×10^{-12} M. All mutants showed slightly more negative ΔG values (−16.18 to −16.35 kcal/mol) and similar or lower Kd values, suggesting comparable or increased BAK binding affinity. HDOCK assigned the wild-type complex a docking score of −251.41 and ligand RMSD of 48.03 Å; all seven mutant complexes had lower scores (−260.82 to −268.85) and lower RMSD values (34.82–34.97 Å), indicating more energetically favorable binding conformations. ClusPro gave a center-weighted score of −672.2 to the wild-type; R215G (−769.2), L235Q (−748.9), G271D (−706.2), W305G (−725.6), and G311D (−769.2) had more negative scores, while V216G (−669.4) and R263S (−641.1) had somewhat fewer negative values. HADDOCK calculated a score of 233.5 ± 34.5 for the wild-type; five mutants—R215G (288.1 ± 14.0), L235Q (284.8 ± 9.0), R263S (278.0 ± 9.6), G271D (248.1 ± 39.1), and V216G (236.4 ± 26.1)—surpassed this value, while W305G (210.5 ± 11.9) and G311D (211.4 ± 7.1) did not. PRODIGY estimated ΔG = −12.8 kcal/mol for the wild-type; five mutants—R215G (−13.6), V216G (−15.6), L235Q (−13.8), R263S (−14.9), and G271D (−14.2)—showed more favorable values, while W305G (−11.4) and G311D (−11.5) had slightly less negative values. R215G, V216G, L235Q, R263S, and G271D were selected for molecular dynamics simulation based on their consistently superior docking profiles across all five platforms.

2.10 Analysis of Molecular Dynamics Simulations

To evaluate structural stability and dynamic characteristics of the five highest-ranked docked complexes relative to the wild-type MCL-1–BAK complex, 100 ns molecular dynamics simulations were performed. RMSD, RMSF, radius of gyration (Rg), and hydrogen bond count were evaluated as measures of structural integrity, residue-specific flexibility, and interfacial compactness (Supplementary file 4). All six complexes achieved trajectory convergence throughout the 100 ns simulation (Figure 5A). The wild-type complex demonstrated RMSD values of 5.0×10^{-7} to 0.602 nm (mean 0.481 nm). R215G exhibited the largest RMSD range (5.0×10^{-7} to 0.621 nm; mean 0.504 nm), indicating marginally reduced stability. The four remaining mutants displayed more constrained profiles: V216G (mean 0.420 nm), L235Q (mean 0.475 nm), R263S (mean 0.440 nm), and G271D (mean 0.461 nm).

RMSF analysis revealed that R215G had the highest average RMSF (0.567 nm; range: 0.235–1.466 nm), while V216G had the lowest (0.281 nm; range: 0.118–0.680 nm), indicating the greatest structural rigidity (Figure 5B). L235Q (mean 0.373 nm), R263S (mean 0.344 nm), and G271D (mean 0.350 nm) demonstrated flexibilities comparable to the wild-type (mean 0.387 nm). Rg analysis showed that all five mutant complexes exhibited marginally reduced mean Rg values relative to the wild-type (2.143 nm): R215G (2.128 nm), V216G (2.063 nm), L235Q (2.094 nm), R263S (2.077 nm), and G271D (2.108 nm), suggesting enhanced interfacial compaction consistent with heightened binding affinities (Figure 5C). Hydrogen bond analysis revealed that the wild-type complex had a mean of 156.4 bonds per frame (range: 131–237). R215G exhibited the lowest average (145.4; range: 120–209) and highest variability. In

contrast, V216G (158.9), L235Q (161.6), R263S (166.1), and G271D (158.1) demonstrated enhanced average hydrogen bond counts relative to both the wild-type and R215G, with reduced inter-frame variation, indicating improved interfacial specificity and structural integrity (Figure 5D).

3.0 Discussion

This study employed a comprehensive computational framework to examine the structural and functional consequences of somatic missense variants in MCL-1 and their effects on the MCL-1–BAK inhibitory complex. Among 146 missense variants, seven high-confidence deleterious mutations (R215G, V216G, L235Q, R263S, G271D, W305G, and G311D) were identified. Five variants (R215G, V216G, L235Q, R263S, and G271D) were selected for molecular dynamics (MD) simulation based on their superior and consistent docking profiles. All five variants destabilized the MCL-1 monomer but maintained or enhanced BAK binding affinity and complex stability, consistent with prior computational analyses of gain-of-function mutations in the BCL-2 family[17,18].

The identification of seven deleterious variants was assessed using SIFT, PolyPhen-2, PROVEAN, SNPs&GO, and PANTHER prioritizing pathogenic variants. PolyPhen-2 values exceeding 0.98 and PROVEAN scores below − 4.5 indicate substantial deleterious potential, while MetaRNN pathogenicity ratings (0.862–0.982) provide additional machine-learning validation. Employing five complementary classifiers significantly reduces false positives, as demonstrated in BCL-2 family mutation screening where multi-tool consensus reliably predicts functional disruption. R263S received the highest pathogenicity scores (PolyPhen-2 = 1.000; PROVEAN = − 5.94; SNPs&GO = 0.821), consistent with its location at the canonical Arg263 ionic anchor of the BH3-binding groove targeted by clinical-stage MCL-1 inhibitors like AZD5991 and S63845[14,56].

All seven variants exhibited negative ΔΔG values across six thermodynamic prediction platforms, consistently indicating MCL-1 monomer instability. V216G produced the greatest destabilization (I-Mutant2.0 ΔΔG = − 3.54 kcal/mol; mCSM = − 2.35 kcal/mol; DynaMut2 = − 2.28 kcal/mol) by removing the valine isopropyl side chain from pocket P3, creating a hydrophobic void that compromises the compact BH-domain scaffold. A similar reported mechanism, whereby a hydrophobic substitution at a P3-adjacent MCL-1 site (V220F) induced a loop-to-helix transition, destabilizing the monomer while altering BAX interactions[17]. W305G also resulted in significant destabilization (DynaMut2 ΔΔG = − 2.90 kcal/mol), attributable to loss of the tryptophan indole side chain critical for hydrophobic core packing. Project HOPE analysis corroborated these observations: R215G, V216G, and R263S introduced smaller side chains causing internal voids and disrupted interface contacts, while L235Q and G271D introduced larger, polarity-inconsistent residues causing steric and electrostatic disturbances within the BH3-helical core. Elevated ConSurf conservation scores (8–9) at five of seven positions indicate strong purifying selection, suggesting mutations at these sites likely disrupt the specialized scaffold required for BAK/BAX sequestration.

GeneMANIA and STRING (confidence score 0.999) confirmed the central role of MCL-1 in mitochondrial apoptosis, identifying direct interactors including BAK1, BAX, BIM, NOXA, BCL-XL, BCL-2, and HUWE1. KEGG pathway enrichment analysis via WebGestalt identified apoptosis (hsa04215; enrichment ratio 106.82; FDR = 5.19×10^{-13}) as the primary pathway, with platinum drug resistance (hsa01524) and p53 signaling (hsa04115) also significantly enriched. The association between platinum resistance[57] and elevated MCL-1 expression[8] is well-established as a mechanism of cisplatin resistance in various tumors, where MCL-1-mediated BAK sequestration restricts mitochondrial apoptosis in response to chemotherapeutic agents. Somatic mutations that enhance the MCL-1–BAK interaction, as observed in all five selected variants, may further contribute to resistance beyond gene amplification. MCL-1 amplification at the 1q21 locus occurs in nearly 40% of multiple myeloma cases[10], whereas gain-of-function mutations represent a distinct resistance mechanism undetectable by standard protein quantification.

Despite MCL-1 destabilization by all variants, molecular docking consistently demonstrated improved or comparable BAK binding affinities relative to the wild-type (PRODIGY ΔG = − 12.8 kcal/mol). The mechanistic basis lies in the distinction between global fold stability and binding-interface stability: mutations that create voids in the hydrophobic core can simultaneously reduce steric hindrance at the binding groove, enabling tighter inter-chain packing[58,59]. V216G exhibited the highest binding energy (PRODIGY ΔG = − 15.6 kcal/mol; Kd = 1.01×10^{-12} M) due to an optimized P3 cavity accommodating the BAK BH3 helix. R263S (PRODIGY − 14.9 kcal/mol) compensates for salt-bridge loss by forming new hydrogen bonds via serine at position 263, preserving BAK contact geometry—an adaptive mechanism consistent with recent findings[8,18], who demonstrated that distributed contacts across the P1–P4 groove maintain high-affinity BAK sequestration. G271D (PRODIGY − 14.2 kcal/mol) alters P2 pocket engagement from hydrophobic to partially electrostatic through novel aspartate–BAK contacts. L235Q (− 13.8 kcal/mol) may establish new hydrogen bonds at the groove floor. R215G (− 13.6 kcal/mol) enhances docking pose accuracy (RMSD 34.82 Å versus 48.03 Å wild-type) by reducing steric clashes at the groove entrance and improving BAK BH3 orientation.

The 100 ns MD simulations corroborated the docking results. Four variants—V216G, L235Q, R263S, and G271D—displayed reduced mean RMSD values (0.420, 0.475, 0.440, and 0.461 nm) compared to the wild-type (0.481 nm), and reduced radius of gyration (2.063–2.108 nm versus 2.143 nm), indicating enhanced interfacial compaction consistent with heightened binding affinities. V216G exhibited the lowest RMSF (0.281 nm), suggesting that the P3 cavity restricts inter-chain mobility and promotes a rigid, compact interface. These results are consistent with prior MD studies of MCL-1 with BH3-domain peptides, where reduced interface RMSF correlated with prolonged complex half-life and increased resistance to BH3-mimetic displacement[60].

Hydrogen bond analysis revealed that R263S formed the highest average number of intermolecular hydrogen bonds (166.1 ± 9.57 per frame) compared to the wild-type (156.4 ± 9.23), demonstrating that the serine substitution establishes a denser hydrogen-bond network involving the serine hydroxyl,

backbone carbonyl, and backbone amine, compensating for the loss of the ionic anchor. Enhanced stability of MCL-1–partner complexes blunt stress-induced apoptosis in hematopoietic cells[61]; the R263S findings suggest groove-remodeling mutations can achieve analogous complex stabilization without MCL-1 overexpression. R215G was the sole exception, exhibiting increased RMSD (0.504 nm) and RMSF (0.567 nm) and a reduced average hydrogen bond count (145.4 ± 9.44), consistent with conformational disorder at the groove entrance following loss of the Arg215 surface anchor. Despite its improved docking geometry, R215G likely results in more transient BAK contacts, mechanistically distinguishing it from the other four variants.

4.0 Methodology

The comprehensive analysis of MCL-1 missense mutations, including identification and characterization, is shown in Fig. 1.

4.1 Acquisition of Protein Sequence and Missense Variant Information

The human MCL-1 protein sequence (UniProt Q07820) was obtained from UniProt[20] (https://www.uniprot.org/) database. Somatic missense mutations of MCL1 were collected from COSMIC[19] (https://cancer.sanger.ac.uk/cosmic; accessed 10 August 2025) and were not listed in ClinVar[21] (https://www.ncbi.nlm.nih.gov/clinvar/; accessed 10 August 2025). All variants were analyzed in silico considering that missense substitutions may alter protein folding, stability, interactions, and function.

4.2 Prediction of Functional Impact of Missense Variants

The functional effects of each amino acid change were assessed using four sequence-based tools. SIFT[22] (https://sift.bii.a-star.edu.sg/) evaluates evolutionary conservation and labels mutations as deleterious (≤ 0.05) or tolerated (> 0.05). PolyPhen-2[23] (http://genetics.bwh.harvard.edu/pph2/) uses conservation, structure, and function data to classify variants as benign (0.00–0.45), possibly damaging (0.45–0.98), or probably damaging (0.98–1.00). PROVEAN[24] (http://provean.jcvi.org) compares wild-type and mutant protein sequences, scoring ≤ − 4.5 as deleterious and higher scores as neutral. SNPs&GO[25] (http://snps.biofold.org/snps-and-go/) uses sequence, conservation, and Gene Ontology data to predict whether variants are disease-associated (≥ 0.5) or neutral (< 0.5). Findings from PANTHER[26] were also referenced.

4.3 Analysis of Protein Thermodynamic Stability

Four tools assessed the thermodynamic impact of each substitution on MCL-1 stability. I-Mutant 2.0[27] (http://folding.biofold.org/i-mutant/i-mutant2.0.html) predicts changes in folding free energy (ΔΔG), with ΔΔG ≥ 0 kcal/mol indicating greater stability and ΔΔG < 0 kcal/mol indicating destabilization. MUpro[28]

(http://mupro.proteomics.ics.uci.edu/) uses neural network and support vector machine algorithms to classify substitutions as stabilizing (score ≥ 0) or destabilizing (score < 0). SAAFEC[29] (http://compbio.clemson.edu/SAAFEC/) estimates ΔΔG for single-point mutations to assess changes in stability. iStable[30] (http://predictor.nchu.edu.tw/iStable/indexSeq.php) combines multiple methods to provide consensus ΔΔG predictions. All tools used the protein FASTA sequence, mutation site, and substituted residue as inputs.

4.4 Evolutionary Conservation Analysis

Evolutionary conservation of wild-type MCL-1 residues was evaluated using the ConSurf server[31] (http://consurf.tau.ac.il/). This tool estimates evolutionary rates from a multiple sequence alignment and a phylogenetic tree of homologous proteins. Residues are graded 1 (very variable) to 9 (highly conserved). Previously identified variants were mapped onto the MCL-1 conservation profile by aligning sequence positions, prioritizing substitutions at constrained sites likely to be functionally or structurally important.

4.5 Evaluation of Structural Consequences of Point Mutations

Project HOPE[32] (http://www.cmbi.ru.nl/hope/) was employed to examine the physicochemical and structural effects of each MCL-1 missense mutation. The server amalgamates three-dimensional protein structural coordinates from the PDB with functional annotations from UniProt and DAS-based predictions, generating comparative reports that elucidate variations in size, charge, hydrophobicity, and secondary-structure propensity between wild-type and mutant residues. Pathogenicity scores from MetaRNN[33], ranging from 0 to 1, were obtained for each mutation, with higher values indicating a greater likelihood of pathogenicity.

4.6 Comparative Structural Modeling of Wild-Type and Mutant Proteins

Mutations affecting the structural stability of MCL-1 were simulated using mCSM[34] (http://structure.bioc.cam.ac.uk/mcsm). This machine learning framework utilizes graph-based atomic distance signatures to predict alterations in Gibbs free energy (ΔΔG values). Mutations were classified as stabilizing or destabilizing based on the sign and magnitude of the predicted ΔΔG. DynaMut2[35] (https://biosig.lab.uq.edu.au/dynamut2/) was employed to assess alterations in conformational flexibility and thermodynamic stability through normal mode analysis (NMA). Predicted free energy changes (ΔG values) below zero were classified as destabilizing, whilst those above zero were regarded as stabilizing. Both tools required the wild-type protein structure in PDB format as input.

4.7 Interaction Network and Pathway Enrichment Analysis

The functional interaction network of MCL1 was investigated using GeneMANIA[36] (http://www.genemania.org), which analyzes genomic and proteomic datasets to identify functionally

associated genes via co-expression profiles, shared pathway involvement, co-localization, protein domain similarity, and established physical interactions. Functional activity acquired these interacted genes from GeneCards[37] (www.genecards.org). Physical protein–protein interaction networks were subsequently established using STRING[38] (https://string-db.org/), with a minimum interaction confidence of 0.999 enforced to retain only robustly supported partnerships. Biological pathway enrichment analysis was conducted using WebGestalt[39] (http://www.webgestalt.org/) to identify significantly over-represented molecular pathways among MCL1-associated genes.

4.8 Homology Modeling of Mutant MCL-1 and Its Structure Validation Using Ramachandran Plot

Experimentally resolved structures of wild-type MCL-1 (PDB: 6OQB) and human BAK (PDB: 7M5B) were retrieved from the RCSB Protein Data Bank[40] (https://www.rcsb.org). Comparative homology modeling in SWISS-MODEL[41] (https://swissmodel.expasy.org/) using templates with the best global model quality estimate yielded mutant conformations of MCL-1. UniProt (ID: Q16611) provided the BAK protein sequence. Each homology model's stereochemical quality was assessed using Ramachandran plot analysis[42], which examines the distribution of backbone dihedral angles across all residues. The PROCHECK[43] validation server (https://www.ebi.ac.uk/thornton-srv/software/PROCHECK/) generated Ramachandran plots for each mutant MCL-1 model. Stereochemically acceptable models had more than 90% of residues in the most favored regions. PyMOL[44] molecular visualization software was used to visualize the mutant models (Fig. 4B). All structures were validated before docking experiments.

4.9 Protein-Protein Molecular Docking

Protein-protein docking of each MCL-1 mutant with wild-type BAK was conducted using five complementary platforms. PPA-Pred2[45] (https://www.iitm.ac.in/bioinfo/PPA_Pred/) and PRODIGY[46] (http://milou.science.uu.nl/services/PRODIGY) both calculated binding free energy (ΔG) and dissociation constant (Kd), where more negative ΔG and lower Kd values indicate stronger binding affinity. HDOCK[47] (https://hdock.phys.hust.edu.cn/) produced docking scores and ligand RMSD values, with lower RMSD values indicating greater pose accuracy. ClusPro[48] (https://cluspro.org/) determined stable binding geometries using cluster-based energy scoring with minimal center-weighted energies. HADDOCK 2.4[49] (https://wenmr.science.uu.nl/haddock2.4/) executed data-driven docking using bioinformatics-derived constraints, where lower scores indicate stronger, more stable complexes.

4.10 Molecular Dynamics Simulation

To track atomic-level movements over time, 100-nanosecond molecular dynamics simulations[50] were performed on the five leading docked complexes to assess flexibility and stability. All simulations used the GROMACS[51] program through the WebGRO[52] platform (https://simlab.uams.edu/), with the CHARMM27[53] force field modeling atomic interactions. Systems were charge-neutralized with 0.15 M NaCl and solvated with a TIP4P[54] water box. Energy minimization was performed over 5,000 steps,

followed by NVT and NPT equilibration at 298 K and 1 bar. During each 100 ns simulation, 1,000 snapshots were saved and subsequently analyzed for RMSD, RMSF, hydrogen bond count, and radius of gyration[55].

5.0 Conclusion

This study investigated whether somatic missense variants in MCL-1 alter its capacity to sequester the pro-apoptotic protein BAK and evaluated the implications for apoptotic resistance. Using a systematic, multi-tier computational pipeline, five variants (R215G, V216G, L235Q, R263S, and G271D) were identified that maintain or enhance BAK sequestration. Of these, R263S is the most clinically significant, as it abolishes the primary pharmacophoric anchor while paradoxically increasing BAK retention. The G271D variant remodels the P2 pocket, shifting it from a hydrophobic to a partially electrostatic environment and thereby compromising existing P2-targeting inhibitor scaffolds. In contrast, the enhanced groove geometries produced by V216G and L235Q present opportunities for the rational design of mutation-specific MCL-1 inhibitors. As the findings are based solely on computational analyses, experimental validation is necessary. Recommended follow-up studies include site-directed mutagenesis, isothermal titration calorimetry, BAK displacement assays, and cellular apoptosis assays in MCL-1-dependent cancer cell lines. Overall, these results advance the mechanistic understanding of MCL-1-mediated apoptotic resistance and provide a structural basis for precision oncology strategies targeting mutation-specific groove conformations in MCL-1-dependent malignancies.

Declarations

Acknowledgement

This study thanks the Department of Microbiology, Jashore University of Science and Technology for its instrumental support. We also thank Dr. Jashim Uddin, Associate Professor, Department of Pharmacy, Jashore University of Science and Technology for his guidance and support throughout the project.

Funding Information

This research didn’t receive any funding

Author Contribution

RSJR performed data curation, formal analysis, bioinformatic analysis, and visualization. TC and HA conceptualized the study, prepared original draft and cross-checked data analyses. DC and MA helped RSJR in data analysis and visualization of the figure and edited the manuscript. FB, MN and MMA helped in data curation and reviewed the manuscript. TC designed the study, supervised all aspects of its execution, managed project coordination, and critically reviewed and edited the manuscript.

Competing interests

The author(s) declare no competing interests.

Declaration of generative AI and AI-assisted technologies in the writing process

During the preparation of this work the author(s) used Gemini v3.0/Paraphrasing service to improve writing quality. After using this service, the author(s) reviewed and edited the content as needed and take(s) full responsibility for the content of the publication.

Data Availability

The raw mutation data were sourced from the COSMIC database (https://cancer.sanger.ac.uk/cosmic). The curated dataset of 146 somatic missense mutations generated and analyzed during this study is included in this published article as Supplementary File 1.

References

1. Vogler, M. *et al.* The BCL2 family: from apoptosis mechanisms to new advances in targeted therapy. *Signal Transduction and Targeted Therapy 2025 10:1* **10**, 91- (2025).
2. Carrington, E. M. *et al.* Anti-apoptotic proteins BCL-2, MCL-1 and A1 summate collectively to maintain survival of immune cell populations both in vitro and in vivo. *Cell Death & Differentiation 2017 24:5* **24**, 878–888 (2017).
3. O'neill, K. L., Huang, K., Zhang, J., Chen, Y. & Luo, X. Inactivation of prosurvival Bcl-2 proteins activates Bax/Bak through the outer mitochondrial membrane. *Genes Dev.* **30**, 973–988 (2016).
4. Kalkavan, H. & Green, D. R. MOMP, cell suicide as a BCL-2 family business. *Cell Death & Differentiation 2018 25:1* **25**, 46–55 (2017).
5. Widden, H. & Placzek, W. J. The multiple mechanisms of MCL1 in the regulation of cell fate. *Communications Biology 2021 4:1* **4**, 1029- (2021).
6. Young, A. I. J., Timpson, P., Gallego-Ortega, D., Ormandy, C. J. & Oakes, S. R. Myeloid cell leukemia 1 (MCL-1), an unexpected modulator of protein kinase signaling during invasion. *Cell Adh. Migr.* **12**, 513–523 (2018).
7. Zhou, T. *et al.* Myeloid cell leukemia-1 is an important predictor of survival and progression of small cell lung cancer. *Ann. Transl. Med.* **8**, 1589–1589 (2020).
8. Sancho, M., Leiva, D., Lucendo, E. & Orzáez, M. Understanding MCL1: from cellular function and regulation to pharmacological inhibition. *FEBS Journal* **289**, 6209–6234 (2022).
9. Bolomsky, A. *et al.* MCL-1 inhibitors, fast-lane development of a new class of anti-cancer agents. *Journal of Hematology & Oncology 2020 13:1* **13**, 173- (2020).
10. Slomp, A. *et al.* Multiple myeloma with 1q21 amplification is highly sensitive to MCL-1 targeting. *Blood Adv.* **3**, 4202–4214 (2019).
11. Fire, E., Gullá, S. V., Grant, R. A. & Keating, A. E. Mcl-1-Bim complexes accommodate surprising point mutations via minor structural changes. *Protein Science* **19**, 507–519 (2010).

12. Craxton, A. *et al.* NOXA, a sensor of proteasome integrity, is degraded by 26S proteasomes by an ubiquitin-independent pathway that is blocked by MCL-1. *Cell Death & Differentiation 2012 19:9* **19**, 1424–1434 (2012).
13. Xiang, W., Yang, C. Y. & Bai, L. MCL-1 inhibition in cancer treatment. *Onco. Targets. Ther.* **11**, 7301–7314 (2018).
14. Wei, A. H. *et al.* Targeting MCL-1 in hematologic malignancies: Rationale and progress. *Blood Rev.* **44**, 100672 (2020).
15. Tokheim, C. & Karchin, R. CHASMplus Reveals the Scope of Somatic Missense Mutations Driving Human Cancers. *Cell Syst.* **9**, 9-23.e8 (2019).
16. Tantawy, S. I., Timofeeva, N., Sarkar, A. & Gandhi, V. Targeting MCL-1 protein to treat cancer: opportunities and challenges. *Front. Oncol.* **13**, 1226289 (2023).
17. Deepak Shyl, E. nesar S. glory, Malgija, B., Iniyan, A. M. & Vincent, S. G. P. Mutation in MCL1 predicted loop to helix structural transition stabilizes MCL1–Bax binding interaction favoring cancer cell survival. *Proteins: Structure, Function and Bioinformatics* **90**, 1699–1713 (2022).
18. Wei, H. *et al.* Deciphering molecular specificity in MCL-1/BAK interaction and its implications for designing potent MCL-1 inhibitors. *Cell Death & Differentiation 2025 32:6* **32**, 991–999 (2025).
19. Tate, J. G. *et al.* COSMIC: the Catalogue Of Somatic Mutations In Cancer. *Nucleic Acids Res.* **47**, D941–D947 (2019).
20. MCL1 - Induced myeloid leukemia cell differentiation protein Mcl-1 - Homo sapiens (Human) | UniProtKB | UniProt. https://www.uniprot.org/uniprotkb/Q07820/entry.
21. Landrum, M. J. *et al.* ClinVar: Public archive of interpretations of clinically relevant variants. *Nucleic Acids Res.* **44**, D862–D868 (2016).
22. Ng, P. C. & Henikoff, S. SIFT: predicting amino acid changes that affect protein function. *Nucleic Acids Res.* **31**, 3812–3814 (2003).
23. Adzhubei, I., Jordan, D. M. & Sunyaev, S. R. Predicting functional effect of human missense mutations using PolyPhen-2. *Curr. Protoc. Hum. Genet.* **Chapter 7**, (2013).
24. Choi, Y. & Chan, A. P. PROVEAN web server: a tool to predict the functional effect of amino acid substitutions and indels. *Bioinformatics* **31**, 2745–2747 (2015).
25. Capriotti, E. *et al.* WS-SNPs&GO: a web server for predicting the deleterious effect of human protein variants using functional annotation. *BMC Genomics* **14 Suppl 3**, 1–7 (2013).
26. Mi, H., Muruganujan, A., Casagrande, J. T. & Thomas, P. D. Large-scale gene function analysis with PANTHER Classification System. *Nat. Protoc.* **8**, 1551 (2013).
27. Capriotti, E., Fariselli, P. & Casadio, R. I-Mutant2.0: predicting stability changes upon mutation from the protein sequence or structure. *Nucleic Acids Res.* **33**, W306–W310 (2005).
28. Cheng, J., Randall, A. & Baldi, P. Prediction of protein stability changes for single-site mutations using support vector machines. *Proteins: Structure, Function, and Bioinformatics* **62**, 1125–1132 (2006).

29. Getov, I., Petukh, M. & Alexov, E. SAAFEC: Predicting the Effect of Single Point Mutations on Protein Folding Free Energy Using a Knowledge-Modified MM/PBSA Approach. *International Journal of Molecular Sciences 2016, Vol. 17, Page 512* **17**, 512 (2016).
30. Chen, C. W., Lin, J. & Chu, Y. W. iStable: Off-the-shelf predictor integration for predicting protein stability changes. *BMC Bioinformatics* **14**, 1–14 (2013).
31. Ben Chorin, A. *et al.* ConSurf-DB: An accessible repository for the evolutionary conservation patterns of the majority of PDB proteins. *Protein Sci.* **29**, 258 (2019).
32. Venselaar, H., te Beek, T. A. H., Kuipers, R. K. P., Hekkelman, M. L. & Vriend, G. Protein structure analysis of mutations causing inheritable diseases. An e-Science approach with life scientist friendly interfaces. *BMC Bioinformatics* **11**, (2010).
33. Li, C., Zhi, D., Wang, K. & Liu, X. MetaRNN: differentiating rare pathogenic and rare benign missense SNVs and InDels using deep learning. *Genome Med.* **14**, 115 (2022).
34. Pires, D. E. V., Ascher, D. B. & Blundell, T. L. mCSM: predicting the effects of mutations in proteins using graph-based signatures. *Bioinformatics* **30**, 335–342 (2014).
35. Rodrigues, C. H., Pires, D. E., Ascher, D. B., David Ascher, C. B. & eduau, unimelb. DynaMut2: Assessing changes in stability and flexibility upon single and multiple point missense mutations. *Protein Science* **30**, 60–69 (2021).
36. Montojo, J., Zuberi, K., Rodriguez, H., Bader, G. D. & Morris, Q. GeneMANIA: Fast gene network construction and function prediction for Cytoscape. *F1000Res.* **3**, 153 (2014).
37. Stelzer, G. *et al.* The GeneCards suite: From gene data mining to disease genome sequence analyses. *Curr. Protoc. Bioinformatics* **2016**, 1.30.1-1.30.33 (2016).
38. Szklarczyk, D. *et al.* STRING v10: protein–protein interaction networks, integrated over the tree of life. *Nucleic Acids Res.* **43**, D447–D452 (2015).
39. Elizarraras, J. M. *et al.* WebGestalt 2024: faster gene set analysis and new support for metabolomics and multi-omics. *Nucleic Acids Res.* **52**, W415–W421 (2024).
40. Bittrich, S. *et al.* RCSB Protein Data Bank: Efficient Searching and Simultaneous Access to One Million Computed Structure Models Alongside the PDB Structures Enabled by Architectural Advances: RCSB Protein Data Bank: Architectural Advances. *J. Mol. Biol.* **435**, (2023).
41. Waterhouse, A. *et al.* SWISS-MODEL: homology modelling of protein structures and complexes. *Nucleic Acids Res.* **46**, W296–W303 (2018).
42. Hollingsworth, S. A. & Karplus, P. A. A fresh look at the Ramachandran plot and the occurrence of standard structures in proteins. *Biomol. Concepts* **1**, 271 (2010).
43. Laskowski, R. A., Rullmann, J. A. C., MacArthur, M. W., Kaptein, R. & Thornton, J. M. AQUA and PROCHECK-NMR: programs for checking the quality of protein structures solved by NMR. *J. Biomol. NMR* **8**, 477–486 (1996).
44. Rosignoli, S. & Paiardini, A. Boosting the Full Potential of PyMOL with Structural Biology Plugins. *Biomolecules 2022, Vol. 12,* **12**, (2022).

45. Yugandhar, K. & Gromiha, M. M. Protein–protein binding affinity prediction from amino acid sequence. *Bioinformatics* **30**, 3583–3589 (2014).
46. Xue, L. C., Rodrigues, J. P., Kastritis, P. L., Bonvin, A. M. & Vangone, A. PRODIGY: a web server for predicting the binding affinity of protein–protein complexes. *Bioinformatics* **32**, 3676–3678 (2016).
47. Yan, Y., Tao, H., He, J. & Huang, S. Y. The HDOCK server for integrated protein–protein docking. *Nature Protocols 2020 15:5* **15**, 1829–1852 (2020).
48. Kozakov, D. *et al.* The ClusPro web server for protein–protein docking. *Nature Protocols 2017 12:2* **12**, 255–278 (2017).
49. Honorato, R. V. *et al.* The HADDOCK2.4 web server for integrative modeling of biomolecular complexes. *Nat. Protoc.* https://doi.org/10.1038/S41596-024-01011-0 (2024) doi:10.1038/S41596-024-01011-0.
50. Karplus, M. & Kuriyan, J. Molecular dynamics and protein function. *Proc. Natl. Acad. Sci. U. S. A.* **102**, 6679–6685 (2005).
51. Yekeen, A. A., Durojaye, O. A., Idris, M. O., Muritala, H. F. & Arise, R. O. CHAPERONg: A tool for automated GROMACS-based molecular dynamics simulations and trajectory analyses. *Comput. Struct. Biotechnol. J.* **21**, 4849 (2023).
52. Ercin, N. *et al.* Investigation of the Effects of Acacetin on Autophagy Pathway and Exosome Release in Amyloid Beta Peptide-Induced Toxicity Models. *Molecular Neurobiology 2025 62:9* **62**, 11030–11046 (2025).
53. Lindahl, E., Bjelkmar, P., Larsson, P., Cuendet, M. A. & Hess, B. Implementation of the charmm force field in GROMACS: Analysis of protein stability effects from correction maps, virtual interaction sites, and water models. *J. Chem. Theory Comput.* **6**, 459–466 (2010).
54. Zielkiewicz, J. Structural properties of water: Comparison of the SPC, SPCE, TIP4P, and TIP5P models of water. *Journal of Chemical Physics* **123**, (2005).
55. da Fonseca, A. M. *et al.* Screening of Potential Inhibitors Targeting the Main Protease Structure of SARS-CoV-2 via Molecular Docking, and Approach with Molecular Dynamics, RMSD, RMSF, H-Bond, SASA and MMGBSA. *Mol. Biotechnol.* **66**, 1919–1933 (2024).
56. Tron, A. E. *et al.* Discovery of Mcl-1-specific inhibitor AZD5991 and preclinical activity in multiple myeloma and acute myeloid leukemia. *Nat. Commun.* **9**, (2018).
57. Lu, X. *et al.* Platinum-Based Mcl-1 Inhibitor Targeting Mitochondria Achieves Enhanced Antitumor Activity as a Single Agent or in Combination with ABT-199. *J. Med. Chem.* **66**, 8705–8716 (2023).
58. Ravichandran, A. *et al.* Structure-guided engineering of protein stability through core hydrophobicity. *Protein Science* **34**, e70360 (2025).
59. Zhou, H. X. & Pang, X. Electrostatic Interactions in Protein Structure, Folding, Binding, and Condensation. *Chem. Rev.* **118**, 1691–1741 (2018).
60. Rasmussen, M. L. *et al.* MCL-1 Inhibition by Selective BH3 Mimetics Disrupts Mitochondrial Dynamics Causing Loss of Viability and Functionality of Human Cardiomyocytes. *iScience* **23**,

101015 (2020).
61. Okamoto, T. *et al.* Enhanced stability of Mcl1, a prosurvival Bcl2 relative, blunts stress-induced apoptosis, causes male sterility, and promotes tumorigenesis. *Proc. Natl. Acad. Sci. U. S. A.* **111**, 261–266 (2014).

Tables

Tables 1 to 5 are available in the supplementary files section

Figures

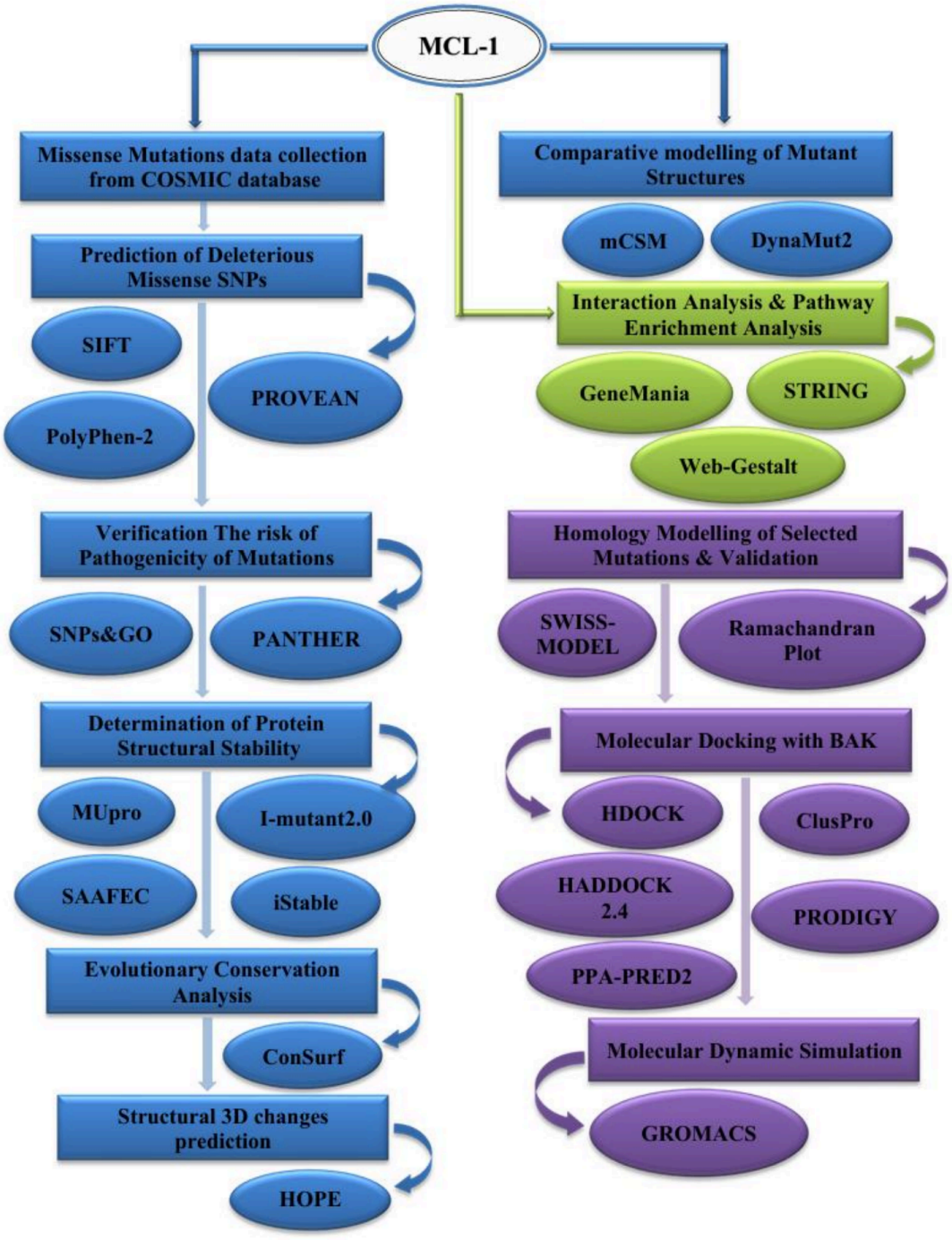


Figure 1

Schematic workflow for the characterization of MCL-1 missense mutations and interaction analysis with BAK. The flowchart outlines the sequential steps used to characterization of missense mutations in the MCL-1. Subsequently, molecular docking and simulations were performed between MCL-1 and BAK to assess mutations that alter BAK sequestration, a key interaction regulating mitochondrial outer membrane permeabilization in apoptosis.

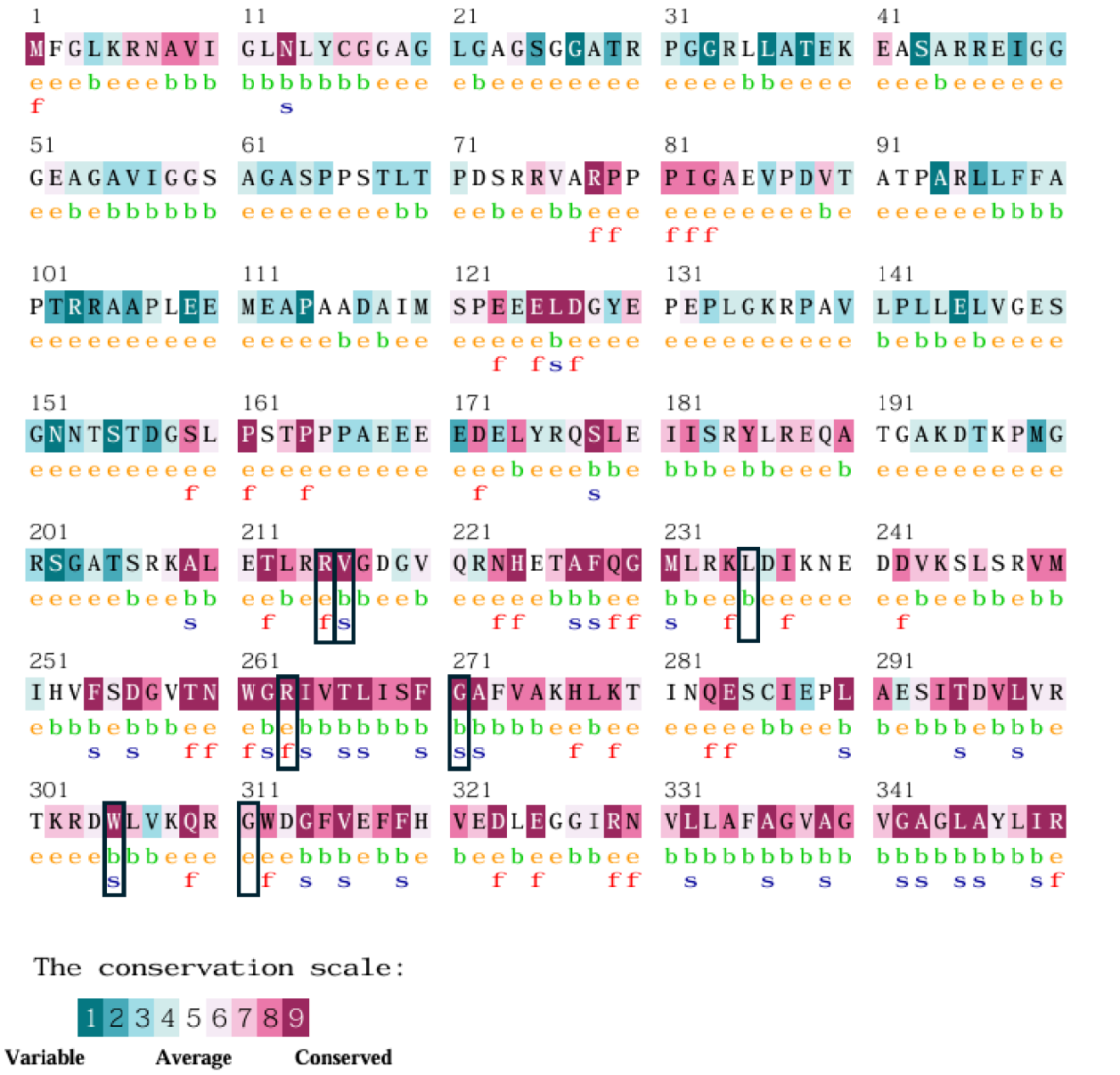


Figure 2

Prediction of evolutionary conserved amino acid residues by ConSurf server. Conservation score is represented as the color-coding bars. Residues are categorized as exposed (e), buried (b), functional (f; conserved and exposed), or structural (s; conserved and buried).

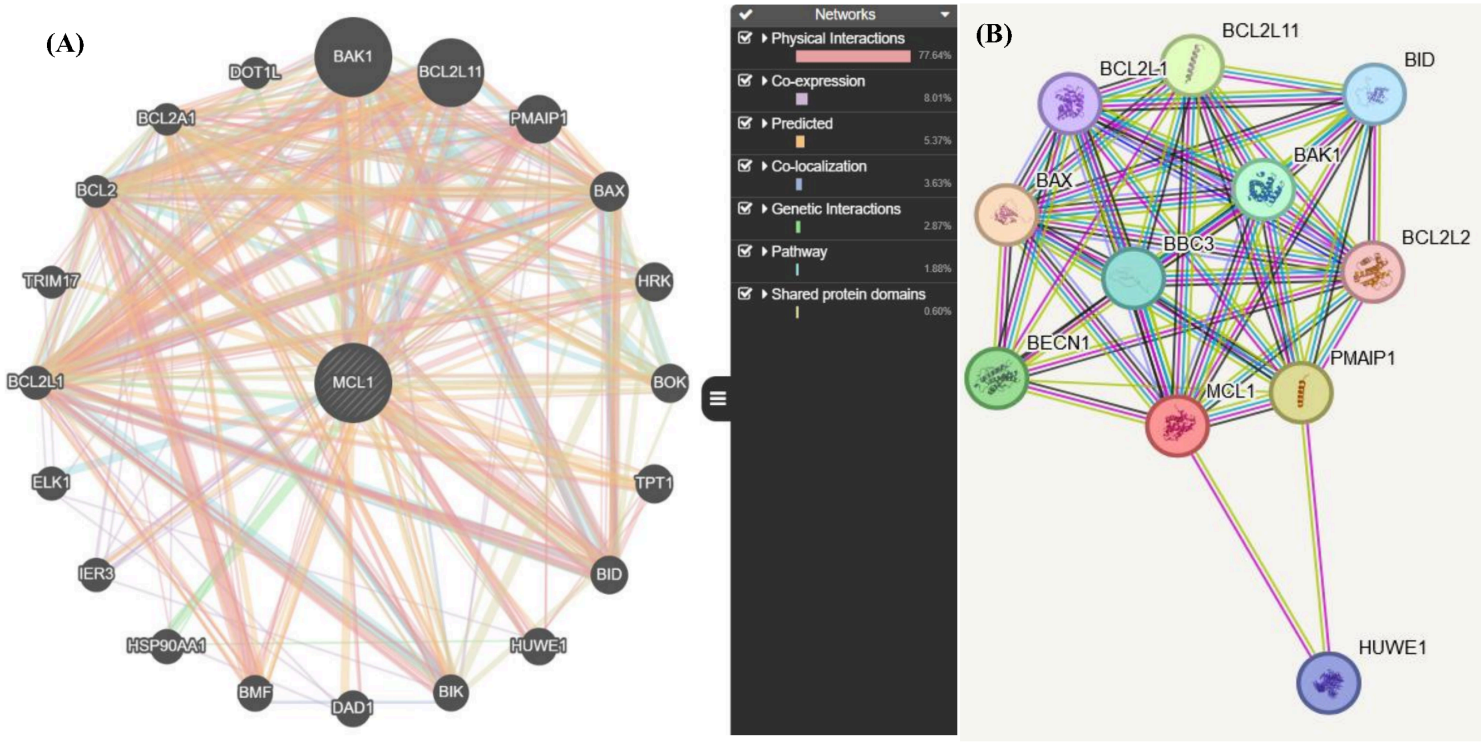


Figure 3

Gene-gene of MCL1 and protein-protein of MCL-1 interactions analysis by GeneMania and STRING. (A) GeneMANIA gene-gene interaction for MCL1 Gene with 20 genes. Different colors of the network edge indicate physical interactions (77.64%), co-expression (8.01%), predicted (5.37%), co-localization (3.63%), genetic interaction (2.87%), pathway (1.88%), and shared protein domain (0.60%). (B) MCL-1 protein interacts with a total of 10 different proteins. Colored nodes: query proteins and first shell of interactors. Empty nodes: proteins of unknown 3D structure (BBC3). Filled nodes: 3D structure is known/predicted. Edges represent protein-protein associations.

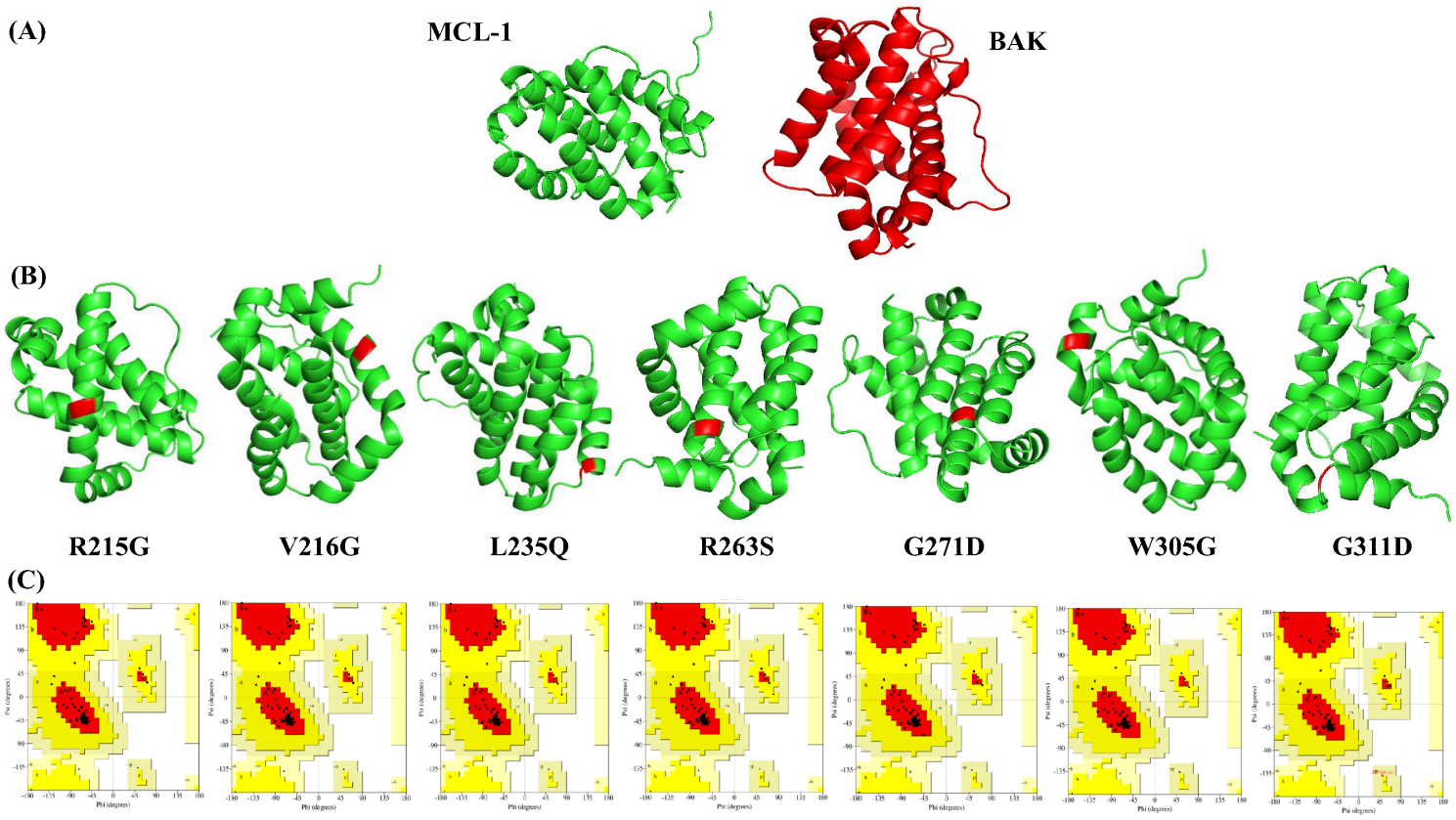


Figure 4

Homology modeling by Swiss-Model, visualization with PyMOL, and protein validation by Ramachandran plot. (A) Three-dimensional structure of wild-type MCL-1 and BAK, visualized using PyMOL. (B) Homology models of selected MCL-1 mutated variants were generated using the Swiss-Model server and SNPs are highlighted in red on the superimposed structures. (C) Ramachandran plot validation of mutant MCL-1 models showing the distribution of phi (φ) and psi (ψ) torsion angles for all residues. Residues in most favored regions are shown in red, while those in additionally allowed regions are shown in yellow.

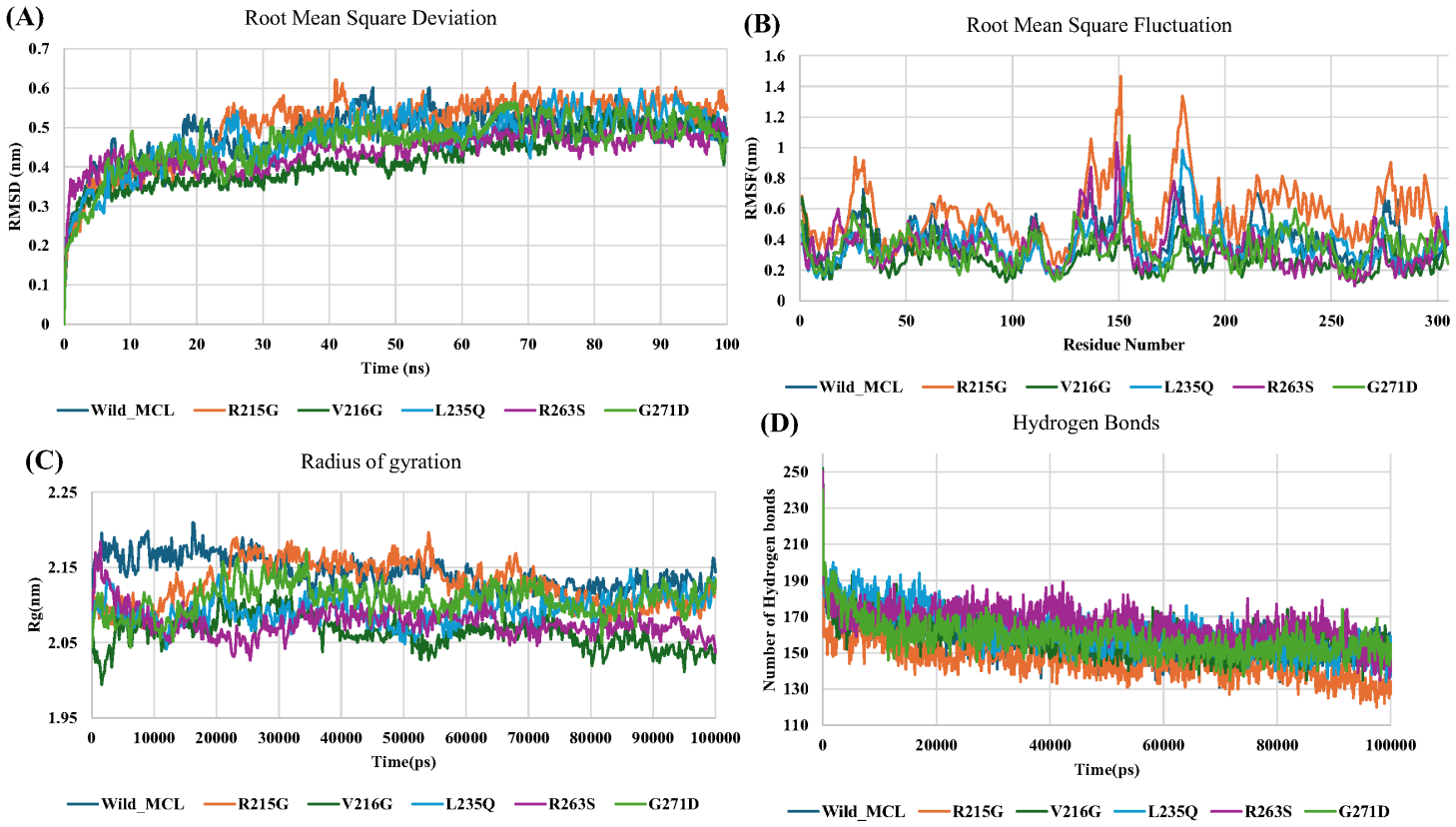


Figure 5

Analysis of RMSD, RMSF, Rg, and H-bonds of native and five mutants of *MCL1* over a 100-ns simulation. (A) Root Mean Square Deviation (RMSD) fluctuations of of Cα atoms of native and mutant structures. (B) RMSF analysis showing variation of Cα atoms of native and mutant structures. (C) Radius of gyration (Rg) analysis represented as a time-dependent change during the simulation. (D) Calculation of H-bonds analysis is represented as a time-dependent process between wild type and mutant proteins for 100ns/100000ps simulation. The color code is as follows: MCL native (blue), R215G mutant (orange), V216G mutant (green), L235Q mutant (light blue), R263S mutant (purple), and G271D mutant (light green).

Supplementary Files

This is a list of supplementary files associated with this preprint. Click to download.

- Supplementaryfile1.xlsx
- Supplementaryfile2.pdf
- Supplementaryfile3.pdf
- Supplementaryfile4.pdf
- Tables.docx